

From Coils to Surface Recession: Fully Coupled Simulation of Ablation in ICP Wind Tunnels

Sanjeev Kumar¹, Alessandro Munafò^{1,2}, Blaine Vollmer¹,
Daniel J. Bodony¹, Gregory S. Elliott¹, Kelly A. Stephani^{1,2},
Sean Kearney¹, and Marco Panesi^{1,2}‡

¹Center for Hypersonics and Entry Systems Studies (CHESS),
University of Illinois Urbana-Champaign, Urbana, IL 61801, USA

²Department of Mechanical and Aerospace Engineering,
University of California Irvine, Irvine, CA 92697, USA

E-mail: mpanesi@uci.edu

Abstract. This work presents a fully coupled, multiphysics computational framework for predicting the thermo-chemical material response of thermal protection systems in inductively coupled plasma (ICP) wind tunnels. The framework integrates a high-fidelity Navier–Stokes plasma solver, an electromagnetic field solver, and a discontinuous-Galerkin material response solver using a partitioned coupling strategy. This enables an *ab initio*, end-to-end simulation of the 350 kW Plasmatron X facility at the University of Illinois Urbana-Champaign (UIUC), including plasma generation, electromagnetic heating, near-wall thermochemistry, and time-accurate material ablation. The model captures key ICP physics such as vortex-mode recirculation, Joule-heating-driven plasma formation, and Lorentz-force-induced flow confinement, and accurately predicts the transition from subsonic to supersonic jet behavior at low pressures. Validation against cold-wall calorimetry and graphite ablation experiments shows that predicted stagnation-point heat fluxes fall well within experimental uncertainty, while fully coupled simulations accurately reproduce measured stagnation temperature histories and recession rates with errors below 12% and 10%, respectively. Remaining discrepancies during early transient heating are attributed to uncertainties in power-coupling efficiency, equilibrium ablation modeling, and material property datasets. Overall, the framework demonstrates strong predictive capability for ICP wind tunnel environments and provides a foundation for improved design, interpretation, and planning of hypersonic material testing campaigns.

‡ Corresponding author (mpanesi@uci.edu).

1. Introduction

In the hypersonic regime, a vehicle traveling at extreme velocities generates a strong bow shock that severely compresses the surrounding gas, resulting in very high post-shock temperatures and imposing stringent thermal loads on the thermal protection system (TPS) [1]. The maintenance of the vehicle's safety and the achievement of mission success depend heavily on the ability of the TPS to withstand intense aerodynamic heating, chemical reactions, and mechanical loads encountered during flight. Given the high cost of testing new thermal protection materials during flight, the aerospace community is heavily relying on specialized ground-based facilities. High-temperature wind tunnels have been developed specifically for this purpose, enabling researchers to expose material samples to controlled, flight-like aerothermal environments and evaluate their performance well before they are ever integrated into a real mission [2,3]. Within the spectrum of ground-based testing facilities, inductively coupled plasma (ICP) wind tunnels occupy a unique role. These systems generate high-enthalpy plasma flows through electromagnetic induction, allowing researchers to recreate key aspects of hypersonic flight within a controlled laboratory setting. Because the plasma is produced without electrodes, the test environment remains exceptionally clean and chemically well-defined, avoiding contamination that could alter material response. ICP facilities can operate in a near-continuous mode while precisely tuning flow properties to match specific mission requirements, including targeted stagnation-point cold-wall heat fluxes and enthalpy levels. This capability makes them valuable for the assessment of thermal protection materials under realistic and high-temperature conditions [4,5].

When exposed to extreme temperatures, the surrounding gas strongly interacts with the vehicle's TPS, leading to substantial surface heating and material loss. This material removal process, known as ablation, can arise from chemical reactions as well as mechanical processes such as erosion or spallation, and may eventually alter the external shape of the TPS. In addition, the gas particles striking the surface undergo catalytic reactions that may play a major role in the overall heat load [6]. Because these coupled chemical and thermal processes strongly influence the performance of a TPS, an accurate modeling of gas-surface chemistry is paramount for the reliable design of hypersonic vehicles. However, simulating the response of a TPS sample to a reacting flow is inherently challenging. The difficulty stems not only from the intricate physics and chemistry governing both the flow and the material surface, but also from the significant uncertainties associated with the predicted flow conditions and the models used to represent these processes. A foundational and still widely adopted approach for modeling thermal response and ablation of a material is the film coefficient method [7–11]. In this framework, surface heating is represented by the enthalpy difference between the boundary layer edge and the wall, scaled by effective heat and mass transfer

coefficients that capture conductive and diffusive fluxes. Ablation rates are calculated assuming surface chemical equilibrium and a specified mass transfer coefficient. The method offers reliable accuracy near stagnation regions and benefits from a decoupled formulation, enabling rapid simulations for preliminary heatshield design. Additionally, it exhibits low sensitivity to wall temperature assumptions, with cold walls and radiative equilibrium conditions yielding comparable heat transfer coefficients. However, the accuracy of the film coefficient approach diminishes away from the stagnation region, primarily due to the emergence of non-equilibrium effects and its limited capability to capture variations in heat and mass transfer coefficients induced by ablation gas blowing [12,13]. Geometric shape changes further complicate the method, as boundary condition profiles become increasingly dependent on the evolution of surface topology [14,15]. Under such conditions, a coupled flow-material solver offers a significant advantage by enabling accurate resolution of time-varying boundary conditions and incorporating non-equilibrium chemistry effects within the boundary layer. As a result, developing robust and efficient flow-material coupling strategies has become an important and active research topic in the hypersonics community [16–22]. These considerations form the basis for the present study, whose objective is to establish a fully coupled numerical framework capable of predicting the response of thermal protection system materials within the environment of an ICP wind tunnel. In particular, this work aims to model the response of a TPS sample in the 350 kW Plasmatron X ICP facility at UIUC and validate the results against recent graphite ablation experiments performed in this facility. Achieving this goal necessitates a comprehensive multiphysics formulation, one that simultaneously models the plasma flow, the electromagnetic field generated by the induction coils, and the complex thermo-chemical and mechanical behavior of the material itself. By integrating these interacting physical processes within a unified computational platform, the framework aims to provide a high-fidelity representation of TPS material behavior under realistic high-enthalpy testing conditions.

Numerical modeling of ICPs involves solving the coupled Navier–Stokes and Maxwell’s equations to capture the plasma’s physico-chemical and electromagnetic behavior. Early studies in the 1960s–1970s modeled the torch as an infinite solenoid under local thermodynamic equilibrium (LTE), simplifying the problem to the coupled solution of the gas energy and induction equations [23–28]. Advances in computational fluid dynamics (CFD) subsequently enabled multi-dimensional magnetohydrodynamic (MHD) simulations [29–38]. During the 1990s and early 2000s, researchers at the Institute for Problems in Mechanics (IPM), Moscow, developed a combined numerical–experimental methodology to determine the catalytic coefficients of TPS samples [39–42]. As part of this approach, which required both detailed experiments and full-facility numerical simulations, IPM researchers were among the first to develop comprehensive simulation frameworks for ICP facilities, modeling the system from the

induction coils to the plasma jet without relying on simplifying assumptions [43, 44]. Nevertheless, these simulations still depended on experimental data to characterize the TPS material response. The present work overcomes this limitation by introducing a fully coupled ICP–material simulation framework. To the author’s knowledge, this study represents the first *ab initio*, end-to-end numerical simulation of an entire inductively coupled plasma facility, spanning from the electromagnetic field generation in the induction coils to the plasma flow and material response, without reliance on experimentally measured input data.

Most existing works on ICP modeling, as highlighted above, still assume LTE conditions, which remain valid at high pressures ($\approx 10^4$ Pa or above) where frequent particle collisions maintain equilibrium, thereby reducing computational cost. However, more recent investigations have revealed that non-local thermodynamic equilibrium (NLTE) effects can become significant at lower pressures [32, 34, 45–50], highlighting the need for more detailed plasma modeling in ICP facilities. The state-to-state approach provides the most accurate treatment of non-equilibrium by resolving each internal energy state as a separate pseudo-species, enabling non-Boltzmann population distributions [47, 49, 51–55]. Despite its fidelity, this method is computationally expensive and depends on extensive atomic and molecular datasets that are not always available. Consequently, simplified models assuming Maxwell–Boltzmann internal state distributions have been developed [56–58], among which the two-temperature (2T) formulation is the most widely used for ICP discharge simulations [56, 57, 59]. This model assumes rapid equilibration between translational and rotational degrees of freedom of heavy particles (*i.e.*, atoms and molecules) while electronic and vibrational modes equilibrate with translation of free electrons. Recent studies employing two-temperature NLTE models for ICP discharges [36, 45, 50, 60–63] underscore the significance of non-equilibrium effects on temperature fields and chemical composition. In this work, the two-temperature NLTE formulation is adopted for the low-pressure simulations where non-equilibrium effects prevail, whereas the high-pressure cases, such as the coupled flow–material response simulations presented in this paper, are modeled under the LTE assumption to describe the plasma within the facility.

The paper is organized as follows: Section 2 provides a concise overview of the multi-solver coupled ICP framework used in this work. Section 3 describes how the material solver is integrated into the ICP framework, enabling end-to-end simulation of the entire facility, from the torch and induction coils through the chamber and up to the test sample. Section 4 provides a detailed description of the Plasmatron X facility and the corresponding simulation setup. Section 5 then presents the overall MHD characteristics within the facility, followed by an analysis of the material response and a comparison with experiments. Conclusions and future work are summarized in Section 6.

2. ICP framework

A complete description of an inductively coupled plasma requires modeling the flow and the electromagnetic field created by the inductor coils. The simulations presented in this work employ a multi-solver coupled numerical framework for ICPs, detailed in ref. [49]. Here, only a concise overview of the framework is provided to contextualize the novel contributions of this work to its advancement. The flow governing equations are solved in a block-structured finite volume (FV) solver, HEGEL (High fidelity tool for maGnEtogas-dynamic appLications) [64], and the electromagnetic (EM) field is solved in a mixed finite element solver, FLUX (Finite-element soLver for Unsteady electromagnetiX) [65]. HEGEL is coupled with the physico-chemical library PLATO [66] for all plasma-related quantities (*e.g.*, transport, thermodynamics), given the flow properties at a given location. The plasma and the electromagnetic field are coupled through the Lorentz force and Joule heating in the fluid momentum equation and energy equations, respectively, and the electrical conductivity in the induction equation. This interaction between the plasma and the electromagnetic solver enables the accurate simulation of intricate magnetohydrodynamic phenomena within ICP wind tunnels. The coupling between HEGEL and FLUX occurs throughout the CFD domain and is called volume coupling. Throughout this paper, this framework is referred to as the “base” ICP framework, emphasizing that it comprises the bare minimum set of solvers required to simulate the Plasmatron X facility.

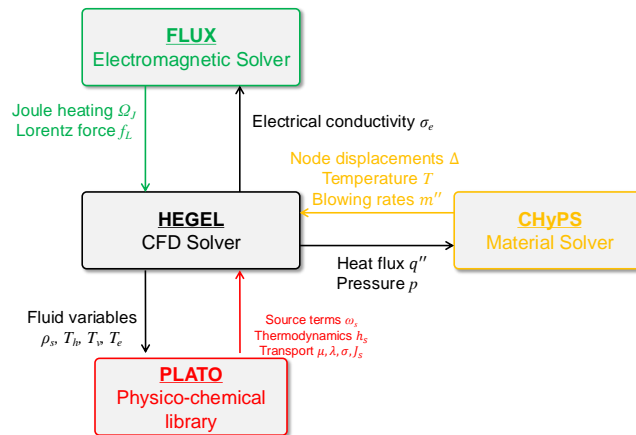


Figure 1: Flowchart of the multiphysics coupled numerical framework used in this work.

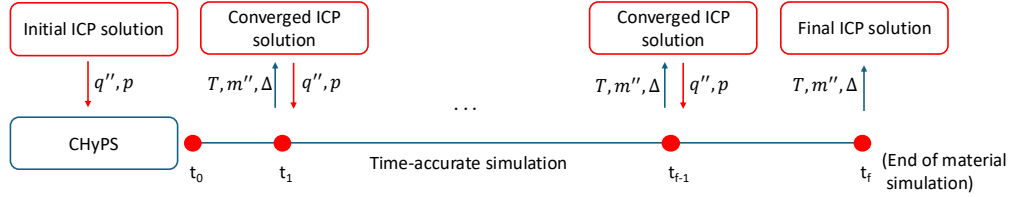


Figure 2: Flowchart of the surface coupling between plasma and material solvers.

3. Coupling of the base ICP framework with material response solver

In this work, the response of the TPS sample in the Plasmatron X facility is modeled with the Coupled Hypersonic Protection System (CHYPS) Simulator [67]. CHYPS is a high-order material response solver based on the discontinuous Galerkin formulation, built on top of the finite-element capabilities of the open-source library MFEM [68]. More details on the governing equations, numerical approach, various capabilities, *etc.*, can be found in ref. [67].

The coupling of the base ICP framework with the material response solver in this work uses a loosely coupled procedure, where the boundary conditions at the sample surface between HEGEL and CHYPS are exchanged at every coupling window. Further, the surface coupling assumes an equilibrium thermo-chemistry, where the plasma simulations are run assuming LTE conditions, while the surface recession modeling in the material solver uses the well-known B' -table approach. This formulation has been implemented in several existing ablation codes (*e.g.*, PATO [69] and KATS [70]), where the dimensionless char ablation mass flux B'_c and wall enthalpy h_w are tabulated as a function of surface pressure, temperature and dimensionless pyrolysis gas mass flux B'_g . More details on the B' ablation modeling in CHYPS can be found in ref. [67]. The TPS sample in the Plasmatron X wind tunnel is generally tested for several seconds. Hence, the numerical simulation of the material needs to run for several seconds to reproduce the material response measured during the experiments. However, running a time-accurate CFD simulation for several seconds is impractical due to the time-step restriction for the simulation. Hence, this work uses a pseudo-steady-state approach for the surface coupling, where the ICP (*i.e.*, HEGEL + FLUX) simulation is run till convergence for the given surface quantities from the material solver at every coupling window. The coupling window in this work is based on the simulation time of the material solver, *i.e.*, the material solver exchanges the surface data with the plasma solver at a fixed simulation time interval. The time interval for the coupling

window is decided based on the gradient of the sample temperature and is changed dynamically during the simulation. Fig. 1 shows the flowchart of the multiphysics coupled numerical framework consisting of the base ICP framework and the material solver, highlighting the various quantities being exchanged. All data exchange between the solvers is managed through PRECICE [71, 72], an open-source coupling library for partitioned multi-physics simulations. The communication between solvers occurs within designated coupling windows, which define when and how data is transferred. These coupling windows are generally distinct and non-overlapping across solvers, as their configurations are tailored to the specific temporal and numerical requirements of each participating solver.

Fig. 2 illustrates the algorithm for coupling between the base ICP framework and the material solver. First, an uncoupled steady-state ICP solution is obtained. HEGEL then passes the surface heat flux (q'') and pressure (p) to CHYPS, which are used as boundary conditions at the sample's active surface to advance the time-accurate material simulation. CHYPS communicates the displacement (Δ) resulting from ablation, surface temperature (T) and blowing rate (m'') back to HEGEL at the next coupling window. HEGEL then makes use of the displacement data to modify the surface boundary of the mesh. The updated coordinates of the surface are then used to modify those of the inner mesh points by means of Linear Transfinite Interpolation (LTI) [73, 74]. The surface temperature and blowing rate data are used in a blowing wall boundary condition [75]. The implementation of this boundary condition relies on the surface normal momentum balance (SMoB) obtained by equating the fluxes normal to the surface from the gas phase to those from the material. When diffusive contributions are neglected, the SMoB relation reads

$$p_\eta = p_f + \rho_f v_f^2 = p_w + \rho_w v_w^2 \quad (1)$$

where p is the gas pressure, and the subscripts w, f , and η denote the wall, flow, and net conditions, respectively. Under LTE conditions, the wall density is retrieved by numerically solving Eq. (1), where the dependence of the wall pressure on the temperature and the sought density is given by the equation of state (*i.e.*, $p = p(\rho, T)$),

$$\rho_w = \frac{m_w''^2}{p_\eta - p_w(\rho_w, T_w)}. \quad (2)$$

Once the wall density is computed, the blowing velocity follows from

$$v_w = \frac{m_w''}{\rho_w}. \quad (3)$$

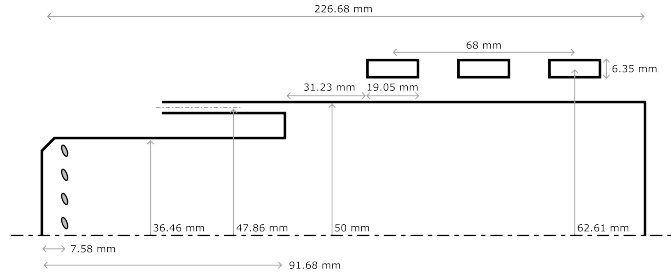


Figure 3: Schematic of the Plasmatron X torch [76].

4. Problem description and simulation setup

The multiphysics computational framework discussed above simulates the 350 kW Plasmatron X facility at UIUC. All the simulations discussed here are 2D axisymmetric. The schematic of the torch section is shown in Fig. 3. The torch has two injectors: central injection consisting of 15 holes, which are inclined 15° downward and have 24° swirl angle, and sheath gas injection consisting of 72 holes and inject gas straight in the axial direction. For simplicity, both injectors are assumed to be continuous annular injectors. The inductor coil has three turns with a rectangular cross-section. In the adopted configuration, the inductor coils are assumed to be parallel to enforce symmetry about the torch axis. The rings are assumed infinitely thin and are located at the midpoint of the innermost part of the coil cross-section, which is a good approximation since most of the current is concentrated there due to the skin-effect [37, 77, 78]. The current running through the set of N_c coils is modeled based on a point-source model as described in ref. [49]. The frequency of the coils for the facility is 2.1 MHz. For all simulations, the central and sheath mass flows are kept fixed at 0.86 g/s and 7.13 g/s, respectively. The only quantities that vary in the experiments and simulations presented in this work are the operating pressure and power. It is important to note that during the facility's operation, only a portion of the operating power is delivered to the plasma, due to various inefficiencies. Hence, the power values used in the simulations are obtained by multiplying the experimental operating power by the corresponding experimentally measured efficiencies (reported for all cases).

The Plasmatron X facility has three kinds of nozzles (attached at its outlet): one straight and two converging-diverging. In this work, only the straight nozzle (of length 129.54 mm and diameter 100 mm) has been considered. Fig. 4 shows the simplified geometry of the entire facility, including the torch, nozzle, chamber, and TPS sample. The TPS sample used in the present calculations is a 30 mm diameter isoQ graphite sample placed at an axial distance of 108 mm from the torch exit as in the experiments. The sample has a holder (100 mm long) which has been assumed to be of the same material (see Fig. 5).

The gas mixture considered for all the simulations is a conventional eleven species air mixture: $\mathcal{S} = \{e^-, N_2, O_2, NO, N, O, N_2^+, O_2^+, NO^+, N^+, O^+\}$. To account for NLTE effects, a conventional two-temperature model is adopted [57], where the heavy particle temperature (T_h) is assigned to the roto-translational degrees of freedom of heavy particles, whereas the *vibronic* temperature (T_{ve}) characterizes the translational energy of free electrons as well as those of the vibrational modes and excited electronic states of heavy particles.

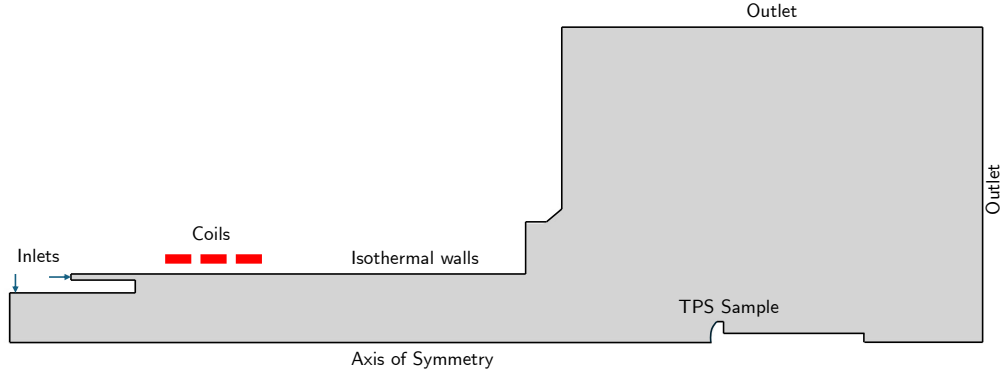


Figure 4: Schematic of the adopted simplified geometry of the Plasmatron X facility consisting of: torch, nozzle, chamber, and TPS sample.

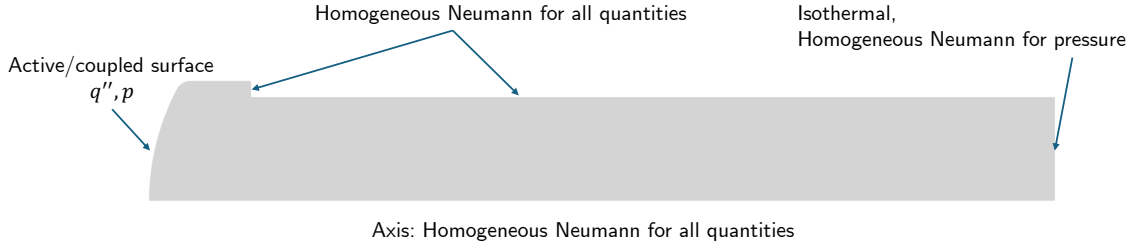


Figure 5: Schematic of the TPS sample geometry (including the holder) with the boundary conditions applied on all surfaces.

4.1. Boundary conditions

4.1.1. *Plasma* The fluid governing equations are solved in HEGEL by imposing the following boundary conditions.

- injectors (subsonic inflow):

$$\rho u = \frac{\dot{m}_x}{A}, \quad \rho v = \frac{\dot{m}_y}{A}, \quad \rho w = \frac{\dot{m}_z}{A}, \quad y_s = y_{s \text{ in}}, \quad \frac{\partial p}{\partial n} = 0 \quad \text{and} \quad T_h = T_{ve} = T_{\text{in}},$$

where the in lower-script denotes the injection conditions. In the above formulas, \dot{m} is the mass flow; A the area of the injector; u , v , and w the axial, radial, and swirl velocity components, respectively; T the temperature; and y_s the mass fraction of species $s \in \mathcal{S}$.

- centerline (symmetry):

$$\frac{\partial \rho_s}{\partial r} = \frac{\partial u}{\partial r} = \frac{\partial p}{\partial r} = 0 \quad \text{and} \quad v = w = 0.$$

- walls (isothermal):

$$u = v = w = 0 \quad \text{and} \quad T_h = T_{ve} = T_w.$$

- Sample surface (blowing wall): as detailed in Section 3.
- outlet (subsonic/supersonic outflow): if the local normal Mach number at the boundary is less than 1, a constant ambient pressure is imposed, $p = p_a$. Conversely, if the local Mach number is greater than 1, the flow properties are extrapolated from the interior.

In all simulations, the temperature at the inlet is set to 300 K. The walls are also assumed at 300 K, consistent with the experimental conditions in which the quartz tube is actively cooled. In practice, the wall temperature may not be maintained exactly at 300 K. However, the plasma field is generally insensitive to modest deviations in the wall temperature.

4.1.2. Electromagnetic field In FLUX, the induction equation is solved by setting the electric field to zero on the symmetry axis and far from the coils: $E(x, 0) = 0$, $E(x, r \rightarrow \infty) = 0$ and $E(x \rightarrow \pm\infty, r) = 0$ [65].

4.1.3. Material Fig. 5 illustrates the boundary conditions applied in CHYPS on the various surfaces of the TPS sample. At the front (*i.e.*, active/coupled) surface, the heat flux (q'') and pressure (p) obtained from HEGEL are prescribed. Along the axis, homogeneous Neumann boundary conditions are imposed for all variables, including temperature and pressure. The same goes for the surface of the sample holder. The back face of the sample holder is instead modeled as an isothermal wall maintained at 300 K, with a homogeneous Neumann boundary condition for pressure.

4.2. Mesh

All simulations in this study employ a point-match, block-structured mesh for HEGEL. The mesh for the torch-chamber-only domain (without the sample) is made of 62 700 cells (with 128 across the torch diameter), while the configuration including the sample contains approximately 58 000 cells (with 90 cells across the torch diameter) (see Fig. 6). These grid resolutions were selected based on a grid-convergence analysis of the plasma flowfield. At the sample surface, the cell thickness was set to $0.8\ \mu\text{m}$, which ensured a grid-converged heat flux.

For FLUX, a structured mesh consisting of around 40 000 rectangular elements was used, as shown in Fig. 7. For the sake of robustness and simplicity, the vertices of the mesh used by FLUX were taken coincident with those of HEGEL in the coupling region (*i.e.*, torch) [49].

Fig. 8 shows the isoQ 30 mm TPS sample mesh used for the material solver. The mesh contains approximately 33 500 elements, with 168 and 88 elements oriented parallel and perpendicular to the active surface within the sample domain, and 200 and 94 elements parallel and perpendicular to the holder surface, respectively. This mesh size was found to be sufficient to attain a grid-converged solution.

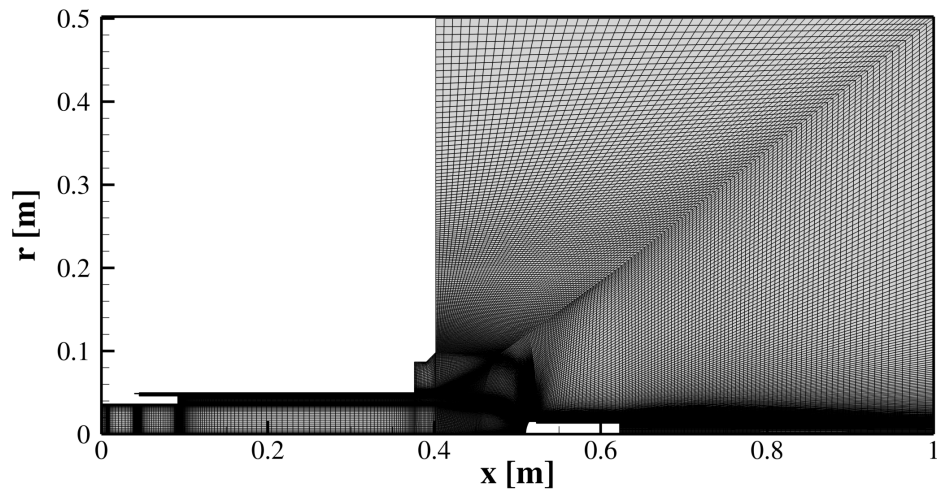


Figure 6: Multi-block structured mesh used by HEGEL.

4.3. Numerical method

The steady-state plasma simulations presented in this work have been performed by integrating the FV discretized flow governing equations by means of the backward

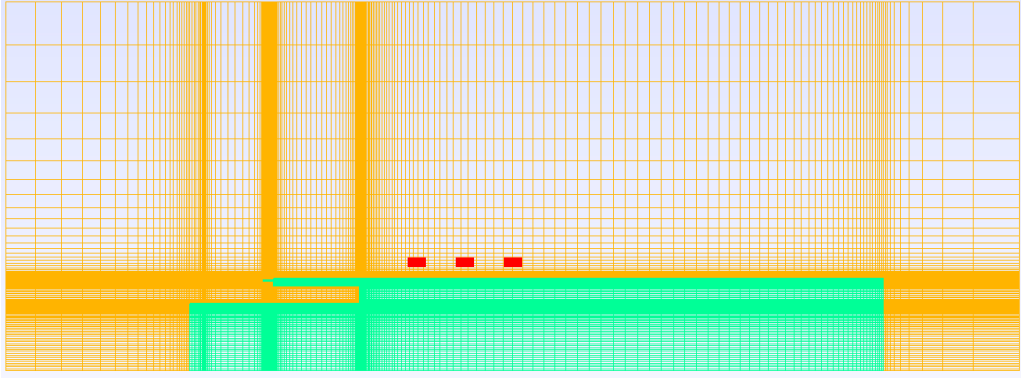


Figure 7: FLUX mesh. The portion of the mesh highlighted in green overlaps with that used in HEGEL (coil locations are marked in red).

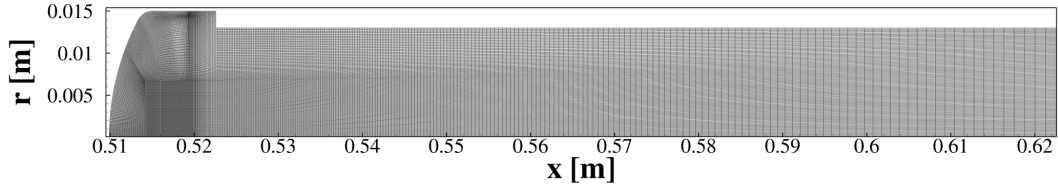


Figure 8: TPS sample (30 mm isoQ) mesh used by CHYPS. The x - y coordinates are defined with respect to the global reference frame employed for the complete computational domain.

Euler method, with CFL-based local time-stepping to accelerate convergence. The simulations were considered converged when the L_2 norm of the solution variation (in terms of conservative variables) decreased by at least 6 orders of magnitude. The plasma solver uses a linear MUSCL reconstruction to achieve second-order accuracy in space [79]. Inviscid fluxes were evaluated using the all-speed AUSM⁺-up flux function [80] to handle the low Mach number stiffness often associated with ICPs. Diffusive fluxes are evaluated using Green-Gauss' theorem to compute face-averaged gradients.

At each coupling window, HEGEL exchanges data with FLUX, which computes the steady-state electromagnetic field based on the given plasma electrical conductivity distribution. To solve the resulting linear system, FLUX employs the Flexible Generalized Minimal Residual (FGMRES) method [81], leveraging Algebraic Multigrid

(AMG) [82] as a preconditioner to enhance convergence.

The governing equations (*i.e.*, gas pressure and temperature equations) in CHYPS are advanced in time using the backward Euler method with a fixed time step of 1 ms. Non-linearities are addressed via Picard iterations.

5. Results

5.1. General features of the plasma inside the Plasmatron X facility

To introduce the main features of the plasma inside the Plasmatron X facility, an LTE simulation of the torch-chamber geometry (without the sample) at 20 kPa, 55 kW and 63.75% efficiency (η) is presented in this section.

Fig. 9 shows the axial velocity and temperature distributions inside the facility. The streamlines added on top of the velocity field highlight a large recirculation bubble in the torch near the inlet, representing a typical vortex-mode discharge. As reported in the literature [37, 83, 84], this phenomenon plays a crucial role in sustaining the hot plasma within the torch. The recirculation bubble carries the hot plasma from the inductor zone back towards the inlet, preventing the plasma from getting swept away by the flow. The plasma is suspended in the middle of the inductor zone, shielded from the tube by a layer of cold fluid coming from the sheath gas injector.

Fig. 10 displays the distribution of Joule heating and Lorentz forces within the torch, predominantly concentrated in the coil region. The large Joule heating in this region raises the temperature of the incoming cold gas, forming a hot plasma core. Additionally, as shown in Fig. 10(b), the radial component of the Lorentz force is directed towards the axis, ensuring that the hot plasma is pushed away from the walls, whereas the axial component, acting in the negative x -direction around $x = 0.2$ m, pushes the plasma towards the inlet. The interplay between the swirling injector and Lorentz forces ultimately generates the large recirculation bubble shown in Fig. 9(a), thereby stabilizing the plasma discharge.

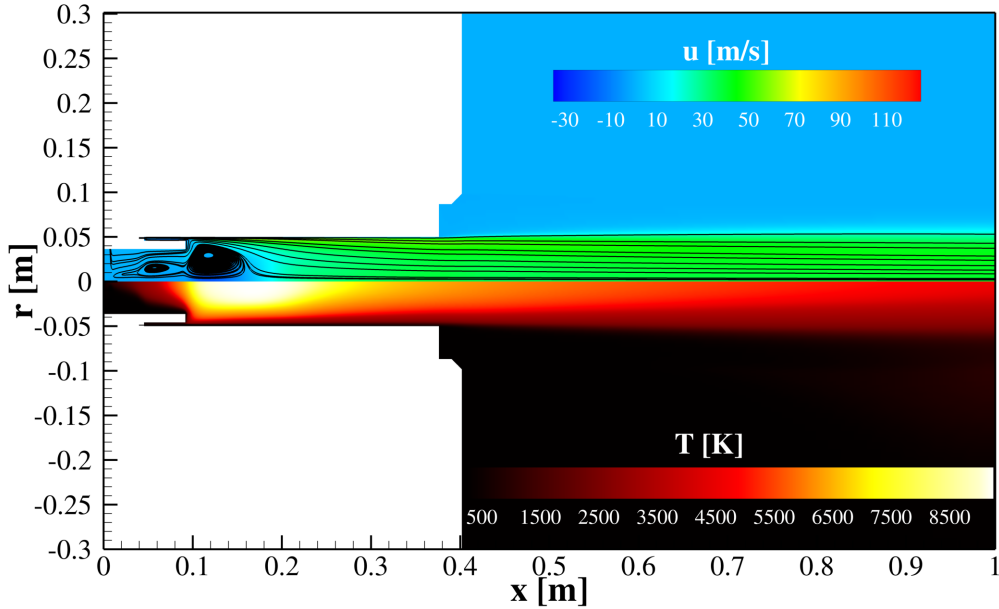


Figure 9: Plasma field inside the Plasmatron X facility. Top: axial velocity with streamlines, bottom: temperature ($p_a = 20$ kPa, $P = 55$ kW, $\eta = 63.75\%$).

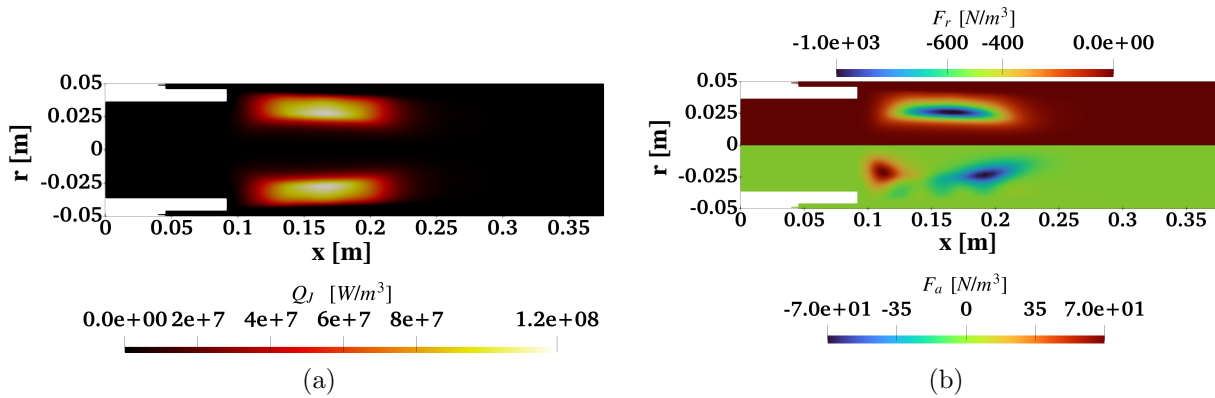


Figure 10: Distribution of the electromagnetic quantities inside the torch. (a) Joule heating, (b) Lorentz force (top: radial component, bottom: axial component) ($p_a = 20$ kPa, $P = 55$ kW, $\eta = 63.75\%$).

Next, a series of simulations was performed at a very low pressure of 600 Pa by varying the power only. This was done to qualitatively validate the current ICP framework by investigating its ability to accurately replicate the transition of the plasma jet in the facility from subsonic to supersonic at very low pressures, a feature

observed in the experiments [85]. This observation aligns with Rayleigh flow theory, which states that heat addition in a constant-area duct drives the flow toward, but not past, sonic conditions. Therefore, at a fixed (very low) operating pressure at which the flow velocities are much higher, a continuous increase in power eventually chokes the nozzle exit, resulting in a supersonic plasma jet in the suddenly expanding chamber region. Hence, a qualitative agreement with the plasma jet transition experiments would not only validate the correct implementation of the models, geometries, etc., but also indicate the correctness of the translation of various operating parameters (*e.g.*, power and efficiency) from the experiments to the simulations. To predict the transition using the current numerical framework, simulations were conducted at five different pressures: 100, 150, 200, 250, and 300 kW, assuming an efficiency of 50 %. Due to the low pressure values, [49], simulations were conducted using the two-temperature NLTE model from Park *et al.* [59].

| Power (kW) | l [Measured] (mm) [85] | l [Predicted] (mm) | Relative error (%) |
|------------|--------------------------|----------------------|--------------------|
| 150 | 68 | 79 | 16.2 |
| 200 | 85 | 103 | 21.2 |
| 250 | 110 | 122 | 10.9 |
| 300 | 120 | 136 | 13.3 |

Table 1: Average distance between shocks in the supersonic plasma jet cases ($p_a = 650$ Pa).

Fig. 11 reports the distributions of heavy-particle temperature and Mach number within the facility at different power levels. The Mach number contours show that the transition from subsonic to supersonic flow occurs around 150 kW, a conclusion further corroborated by the shock-diamond structures in the temperature distribution. Fig. 12 shows the centerline profiles of heavy-particle temperature for various power levels at 600 Pa ambient pressure. The reported axial distance is measured from the nozzle exit. At 100 kW, the absence of a temperature peak suggests a subsonic plasma jet. However, beginning at 150 kW, distinct temperature peaks emerge, indicating the formation of shocks within the jet. At higher power levels, the number of peaks increases, and their positions progressively shift downstream. Additionally, both the spacing between successive shocks and their intensity (reflected by peak amplitudes) grow with increasing power. These trends are consistent with the observations reported in ref. [85], where similar patterns were deduced from plasma light-intensity profiles. A comparison between the simulated and measured average shock spacings, presented in Table 1, shows a good overall agreement. Given the strong correlation between

radiative intensity and plasma temperature, such qualitative similarity in their profiles is expected. Thus, the numerical simulations demonstrate strong qualitative agreement with the experimental results.

It is worth mentioning that a quantitative comparison with the experimentally determined intensity profiles would require coupling the plasma dynamics and radiation. This effort is currently underway, with the ICP framework being integrated with the MURP radiation transport solver [86]. Moreover, ongoing efforts are focused on acquiring more quantitative plasma measurements, such as temperatures, number densities, and velocities, using advanced diagnostic techniques including Coherent Anti-Stokes Raman Scattering (CARS), Optical Emission Spectroscopy (OES), and Laser-Induced Fluorescence (LIF). These state-of-the-art diagnostics will allow for a more rigorous and quantitative validation of the simulation framework in the near future.

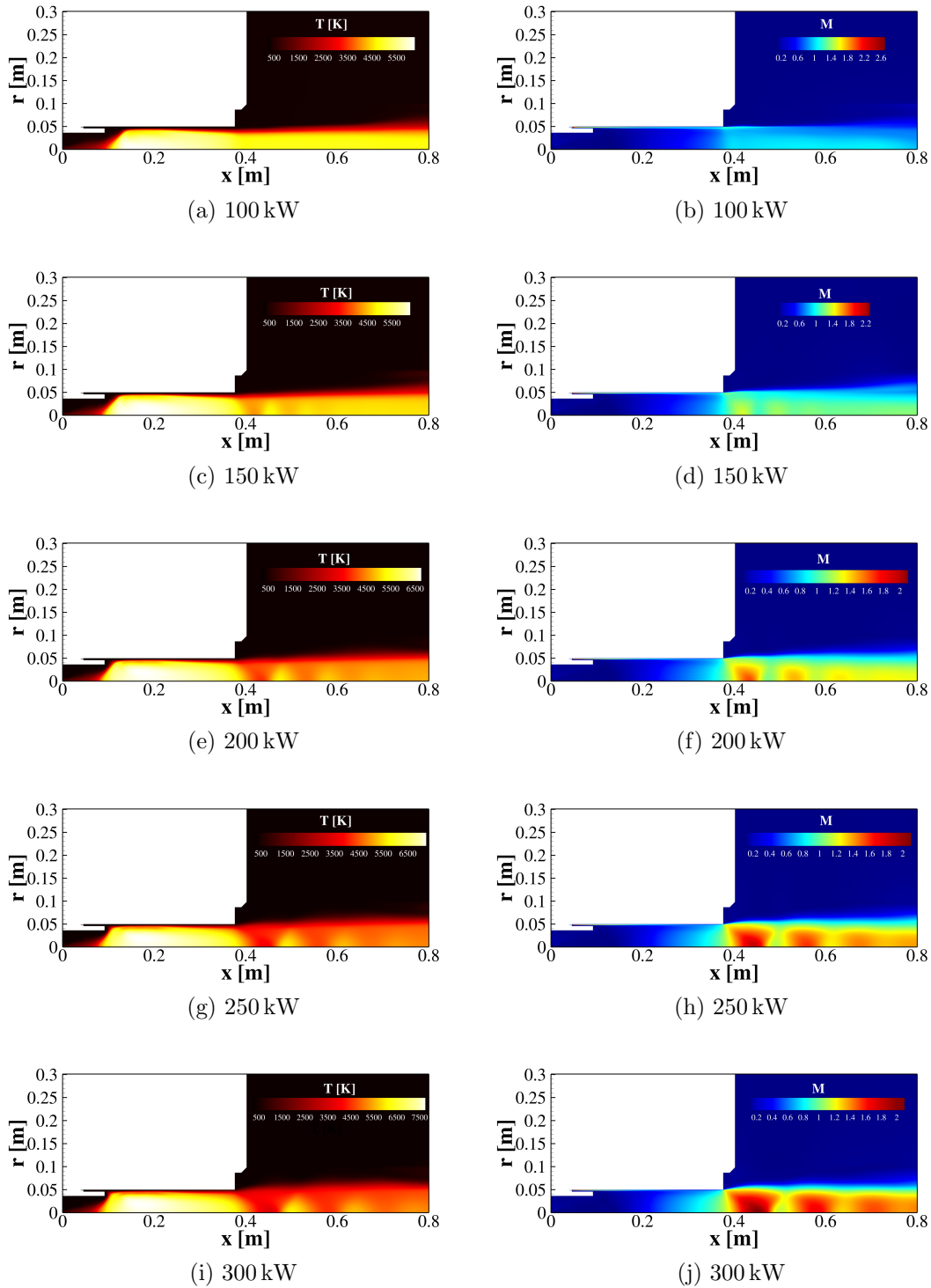


Figure 11: Heavy-particle temperature (a,c,e,g,i) and Mach number (b,d,f,h,j) distributions inside the facility at different power levels and fixed operating pressure and efficiency ($p_a = 600$ Pa and $\eta = 50\%$, respectively), highlighting the subsonic-supersonic transition of the plasma jet.

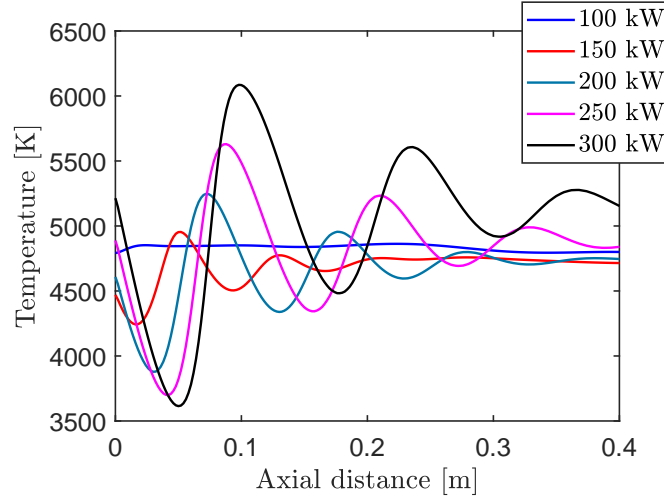


Figure 12: Centerline heavy-particle temperature profiles at different power levels ($p_a = 600$ Pa). The axial distance is measured from the nozzle exit.

5.2. Comparison against cold wall heat flux measurements

This section provides a comparison of the cold wall heat flux predicted by the numerical simulations with the values measured using an in-house copper slug calorimeter probe. More details on the setup of the slug calorimeter can be found in ref. [87]. The measurements used an isoQ 30 mm diameter slug calorimeter (same as the TPS sample geometry discussed in Section 4) placed at an axial distance of 108 mm from the torch exit. Table 2 provides the operating conditions for which the measurements are reported in this paper. It is worth noticing that the operating pressures in all three cases are sufficiently large to justify the use of an LTE plasma model.

| Case | Pressure (kPa) | Power (kW) | Efficiency (%) | q [Measured] (W/cm ²) | q [Predicted] (W/cm ²) | Relative error (%) |
|------|----------------|------------|----------------|-----------------------------------|------------------------------------|--------------------|
| 1 | 20 | 55 | 63.75 | 146.18 | 116.10 | 20.5 |
| 2 | 10 | 55 | 60.16 | 118.29 | 94.20 | 20.3 |
| 3 | 5.5 | 55 | 58.63 | 106.15 | 90.20 | 15.0 |

Table 2: Plasmatron X operating conditions for the cold wall heat flux measurements.

Fig. 13 shows a comparison of the cold wall stagnation heat flux at different pressures (corresponding to cases 1, 2, and 3) at 55 kW power. For all cases, the simulation results fall within the 20% experimental error bars. It must be borne in

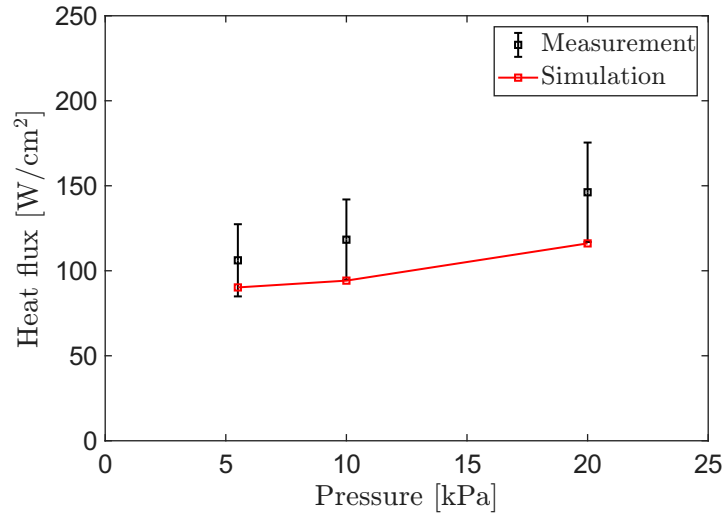


Figure 13: Stagnation cold wall heat flux at various pressure levels ($P = 55$ kW). The measured values have been shown with 20% error bars.

mind that a 20% error is considered a good agreement as a result of the large variability to which heat flux measurements are subjected. In fact, in a slug calorimeter, the heat flux is not measured directly. Instead, it is deduced from the temporal gradient of the temperature recorded by a thermocouple mounted on the rear face of the slug. Consequently, multiple error sources must be rigorously assessed to ensure that the heat-flux estimation derived from this temperature history is reliable. For example, the inferred heat flux is sensitive to the slug diameter (as demonstrated in ref. [88]), which introduces geometric uncertainties. Thermal losses at the interface between the slug and its holder also contribute to errors, since the theoretical model used to back-calculate heat flux assumes adiabatic conditions on all slug surfaces, except the front face exposed to the incident heat. Such idealized conditions are difficult to achieve in practice, and deviations can lead to systematic under- or over-predictions of the heat flux. In addition, the plasma jet impinging on the calorimeter typically exhibits a non-uniform spatial distribution that depends on operating conditions (*e.g.*, mass flow, ambient pressure) and on the probe geometry itself. This non-uniformity can further distort the measured heat flux. Moreover, in an equilibrium boundary layer, as assumed in the numerical simulations, the surface catalycity of the sample has little influence on the heat flux because recombination occurs upstream, and the associated energy is transferred to the gas before reaching the wall. In contrast, for a non-equilibrium boundary layer, the recombination and diffusion time scales are comparable, making the heat flux strongly dependent on surface catalycity (a property that exhibits large variability). It is also important to note that absorptivity, catalycity, and the convective contribution to the heat flux all depend on the instantaneous surface

temperature. Therefore, the net heat flux can vary significantly during tests with relatively long exposure durations. A detailed quantification of these error sources is given in ref. [87]. By contrast, the heat flux obtained from numerical simulations is computed directly from the local spatial temperature gradient, bypassing the indirect estimation procedure used in experiments. Therefore, exact agreement between the two approaches is unlikely until the dominant experimental uncertainties are fully resolved and more consistent measurement–simulation comparisons are established, an area of ongoing research. Nevertheless, the reported comparisons show that the overall heat flux trends are reasonably well captured, which is encouraging and motivates further complex numerical analysis of TPS sample testing in the Plasmatron X facility.

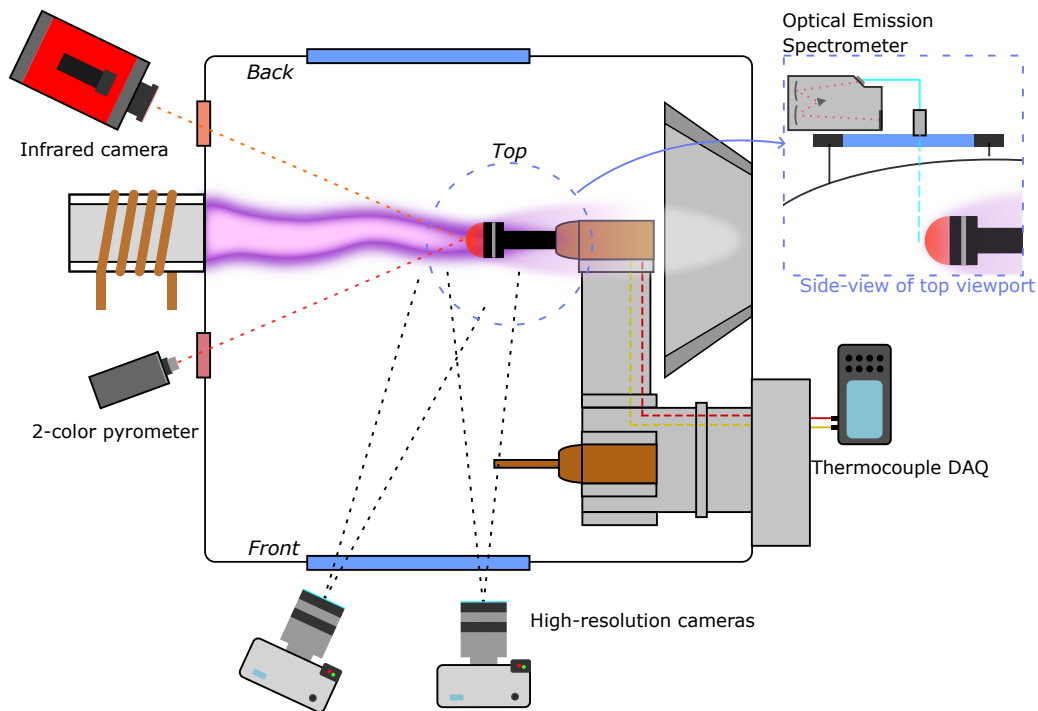


Figure 14: Schematic top-view of the Plasmatron X chamber depicting the available optical accesses and the in situ diagnostic suite [89].

5.3. Material response modeling in Plasmatron X environment

Fully coupled simulations, using the framework discussed in Section 3, have been performed for TPS samples tested in the Plasmatron X facility and compared with the corresponding experimental data. The experiments utilized an isoQ 30 mm graphite (Mersen 2340) sample placed at an axial distance of 108 mm from the torch exit, for which the temporal evolution of stagnation-point surface temperature and recession was measured. The set of operating conditions remains the same as in Table 2.

Fig. 14 shows the simplified schematic of the Plasmatron X chamber along with the typically used instrumentation suite [89]. Surface recession was measured using two high-resolution cameras positioned behind the front viewport. Videos recorded at 60 fps with an effective pixel resolution of approximately $40\ \mu\text{m}$ were analyzed frame-by-frame, with the orthogonal view used to extract stagnation-point recession. Edge detection was applied to identify the surface profile, followed by a least-squares circular fit to mitigate local surface irregularities near the stagnation point prior to recession estimation. A two-color pyrometer, aligned with the stagnation point, simultaneously recorded temperature histories at 100 Hz. Together, these diagnostics enabled time-resolved characterization of stagnation-point recession and surface temperature evolution under plasma exposure. More details on the experimental setup can be found in ref. [89].

The graphite sample simulations in this work employ the material properties of Mersen 2160, modeled with isotropic, temperature-dependent behavior and a constant density of $1.84\ \text{g/cm}^3$. Fig. 15 shows the temperature dependence of thermal conductivity and heat capacity for the graphite sample. The surface emissivity is assumed to remain constant and equal to 0.85. It should be noted that the simulations employ material properties corresponding to a different graphite grade (Mersen 2160) than those used in the experiments (Mersen 2340), due to the unavailability of the data for the latter. Nevertheless, the two grades are expected to exhibit sufficiently similar properties to justify the use of Mersen 2160 data in the simulations.

| Time (s) | Coupling window (s) |
|----------|---------------------|
| 0 | 0.1 |
| 5 | 1 |
| 50 | 5 |

Table 3: PRECICE coupling window schedule between HEGEL and CHYPS.

Simulations were run for 200 s for the TPS sample, while tracking the evolution of the stagnation temperature and surface recession. Table 3 shows the coupling window schedule used for data communication between HEGEL and CHYPS. Fig. 16 presents the plasma and sample temperature fields at $t = 0\ \text{s}$ and $t = 200\ \text{s}$ in the region surrounding the sample for case 1. Initially, the sample is uniformly at 300 K. As the simulation progresses, the surface temperature of the sample rises steadily as a result of the intense thermal loading from the plasma. This heating leads to material ablation, wherein the surface layers of the graphite sample gradually erode as a result of sublimation and mass loss under high temperatures. The effect of this surface recession is clearly visible in the contours at $t = 200\ \text{s}$, showing a noticeable change in geometry. Additionally, the plasma boundary layer is observed to shift slightly outward from

the sample surface, a hallmark of strongly coupled flow–material interactions. This displacement occurs because the ablated gaseous products emerging from the receding surface introduce a blowing effect, which locally alters the near-wall flow and modifies the plasma–surface heat and momentum transfer characteristics.

Fig. 17 through Fig. 19 report the temporal evolution of the stagnation-point temperature and surface recession for all three cases. For case 1, the predicted temperature evolution exhibits excellent agreement with experimental measurements throughout the entire duration. It is important to note that the thermocouple begins recording data only once the temperature exceeds approximately 1000 K. Hence, the measured temperature curve remains flat during the initial phase. Beyond this point, the simulated temperature profile closely follows the experimental trend, with the relative deviation at the final time ($t = 200$ s) being only 3.3%. For cases 2 and 3, a noticeable discrepancy is observed during the early transient period, the possible source of which is addressed in the next section. Nevertheless, as the system approaches steady state, the predicted stagnation-point temperatures are in excellent agreement with the experimental data, with relative errors of 5.9% and 11.2% at $t = 200$ s, respectively. The surface recession histories for all three cases also demonstrate good consistency between simulations and experiments. The relative errors in the predicted steady-state recession rates remain below 10% in all cases, specifically 9.83%, 4.60%, and 5.42% for cases 1, 2, and 3, respectively. A detailed quantitative comparison of the stagnation-point temperature and surface recession rates for all three cases is given in Tables 4 and 5.

| Case | Pressure (kPa) | Power (kW) | Efficiency (%) | T [Measured] (K) | T [Predicted] (K) | Relative error (%) |
|------|-------------------|---------------|-------------------|---------------------|----------------------|-----------------------|
| 1 | 20 | 55 | 63.75 | 1745.1 | 1802.7 | 3.3 |
| 2 | 10 | 55 | 60.16 | 1908.4 | 1794.8 | 5.9 |
| 3 | 5.5 | 55 | 58.63 | 1927.3 | 1711.3 | 11.2 |

Table 4: Summary of the stagnation point temperature comparison with experimental data at $t = 200$ s.

| Case | Pressure (kPa) | Power (kW) | Efficiency (%) | Recession rate [Measured] (μm) | Recession rate [Predicted] (μm) | Relative error (%) |
|------|-------------------|---------------|-------------------|--|---|-----------------------|
| 1 | 20 | 55 | 63.75 | 6.10 | 5.50 | 9.83 |
| 2 | 10 | 55 | 60.16 | 6.08 | 5.80 | 4.60 |
| 3 | 5.5 | 55 | 58.63 | 6.45 | 6.10 | 5.42 |

Table 5: Summary of the stagnation point recession rate comparison with experimental data.

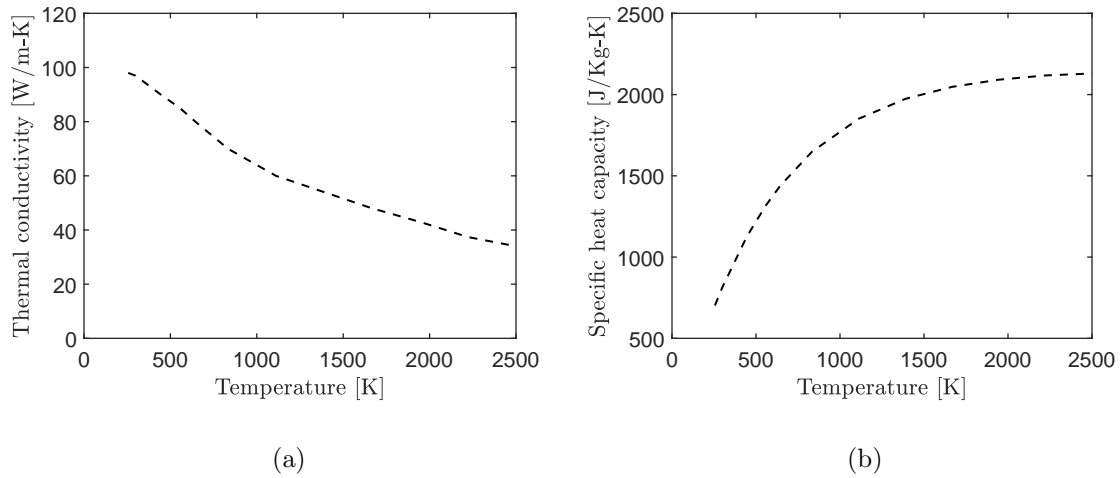


Figure 15: Thermal properties of Mersen 2160 graphite used in this work: (a) thermal conductivity, (b) heat capacity per unit mass.

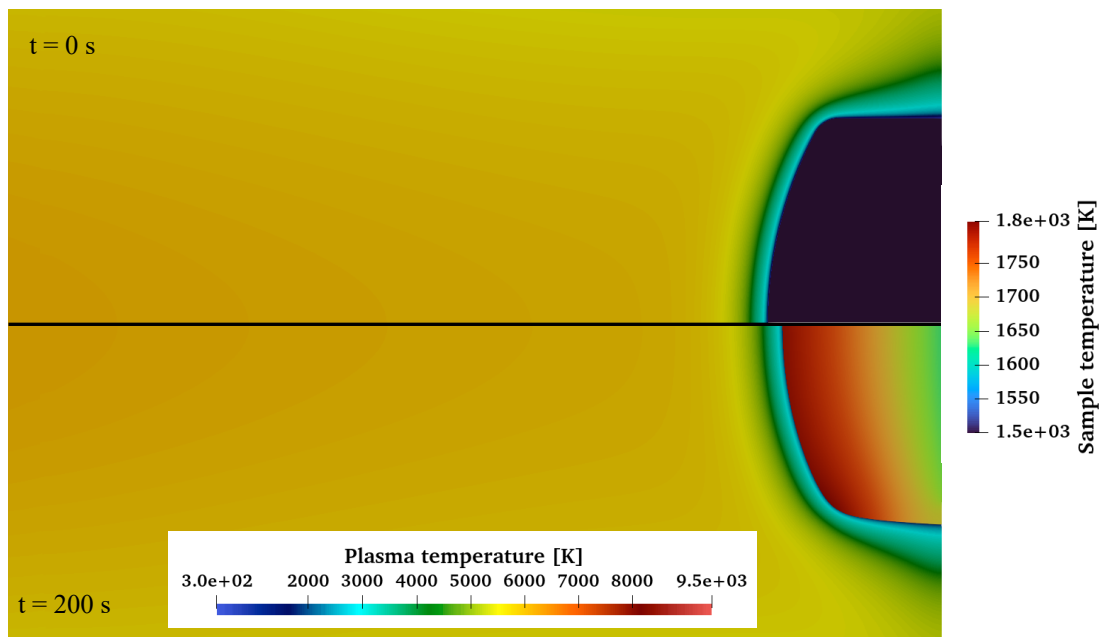


Figure 16: Plasma and sample temperature fields at $t = 0$ and $t = 200$ s for case 1 ($p_a = 20$ kW, $P = 55$ kW, $\eta = 63.75\%$).

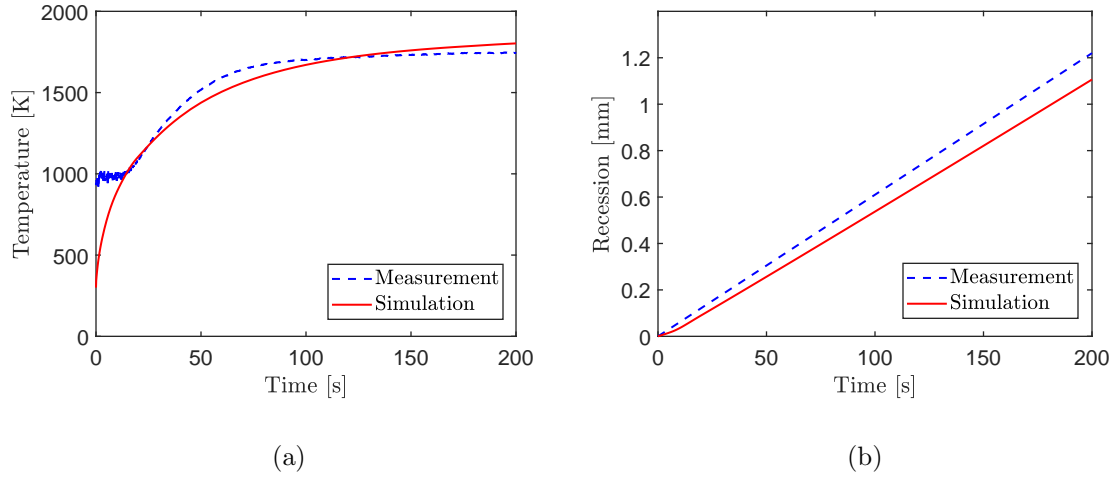


Figure 17: Comparison of the predicted and measured surface stagnation temperature and recession for case 1 ($p_a = 20$ kPa, $P = 55$ kW, $\eta = 63.75$ %).

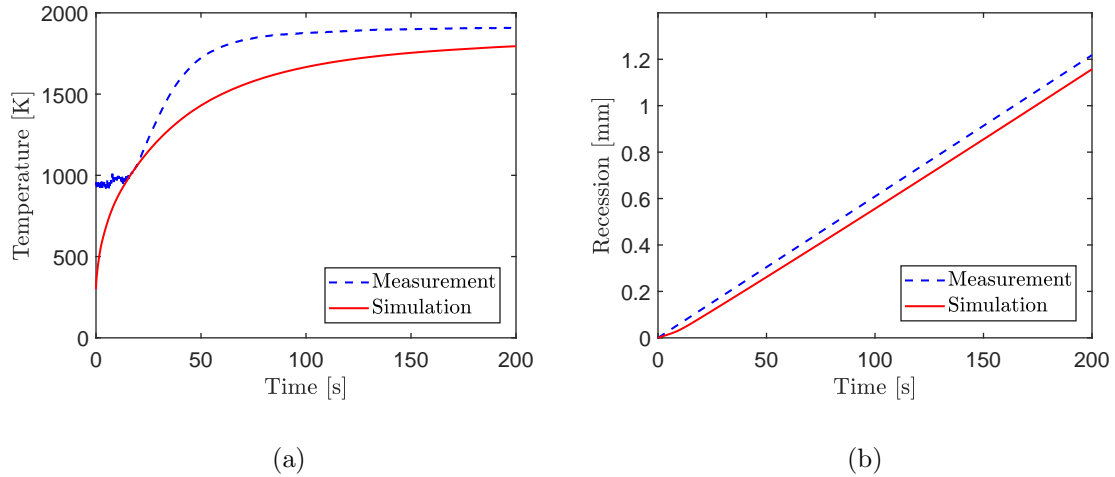


Figure 18: Comparison of the predicted and measured surface stagnation temperature and recession for case 2 ($p_a = 10$ kPa, $P = 55$ kW, $\eta = 60.16$ %).

5.4. Discussion on fully-coupled ablation results

The excellent agreement observed in the ablation predictions (within a relative error of around 10%) is particularly remarkable given the *ab initio* nature of the simulation framework used in this work. To the best of the authors' knowledge, this represents the first *ab initio*, end-to-end numerical simulation of an entire ICP facility, spanning

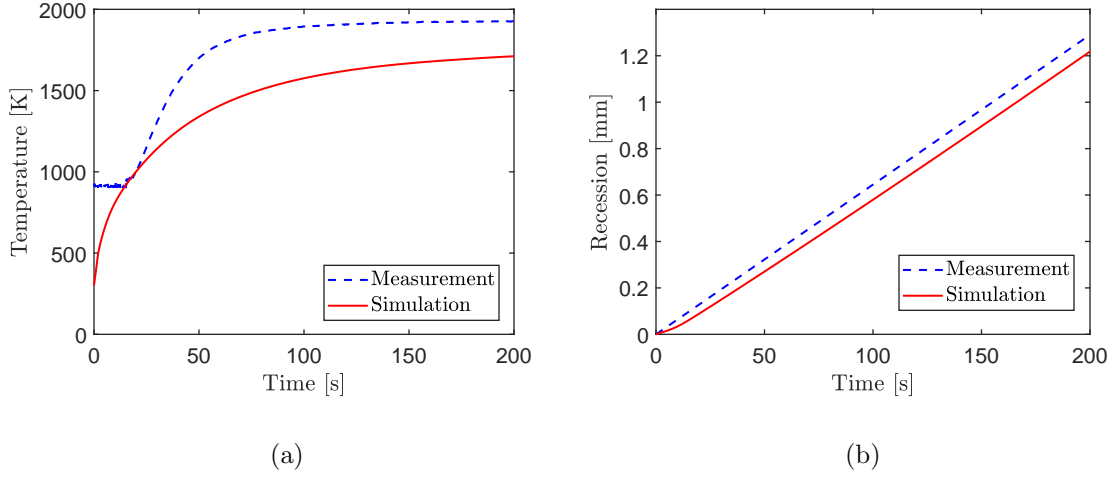


Figure 19: Comparison of the predicted and measured surface stagnation temperature and recession for case 3 ($p_a = 5.5$ kPa, $P = 55$ kW, $\eta = 58.63$ %).

from the electromagnetic power deposition in the coils to the material response of the test sample, and driven exclusively by independently measured facility operating conditions such as input power, chamber pressure, and system efficiencies. Crucially, the framework achieves this level of agreement without any form of parameter tuning, empirical adjustment, or ad-hoc calibration. This approach marks a decisive departure from prevailing practices in the literature, where key parameters, most notably coupling efficiency or effective power, are routinely treated as adjustable quantities and iteratively modified to enforce agreement with experimental measurements [22, 90]. A similar reliance on experimentally prescribed boundary conditions is common in arc-jet simulations, where measured nozzle-exit flow profiles are imposed directly as inlet conditions, thereby bypassing the need to model the facility itself [21]. In contrast, the present framework preserves the predictive integrity of the simulations by relying solely on physics-based models and measured inputs. By eliminating such dependencies, the methodology presented here establishes a genuinely predictive modeling capability for ICP facilities, enabling rigorous assessment of material response and ablation behavior without recourse to empiricism.

Minor deviations are observed in the early transient evolution of the stagnation-point temperature. Given the fully coupled, end-to-end nature of the present multiphysics framework, which simultaneously resolves plasma flow, electromagnetic power deposition, and material response, such discrepancies are not unexpected. Small uncertainties introduced at individual modeling stages can propagate through the coupled system and modestly influence the predicted thermal response during the initial

transient. The dominant contributors to these deviations include uncertainties in the facility coupling efficiency, simplified assumptions in the surface ablation model, and limited availability of material property data. The coupling efficiency, which governs the fraction of radio-frequency (RF) generator power transferred to the plasma, is inherently difficult to quantify and may vary with operating conditions, leading to modest uncertainty in the effective plasma energy input. Additionally, surface ablation is modeled using an equilibrium B' -table formulation, which, while well-suited for steady-state conditions and high-pressure operation, may not fully capture transient finite-rate effects during the onset of ablation. Finally, minor discrepancies may also arise from the use of thermophysical property data corresponding to a closely related graphite grade rather than the exact material tested experimentally.

Addressing these secondary sources of uncertainty through refined facility characterization, finite-rate ablation modeling, and material-specific property calibration constitutes a natural extension of the present work, but is not essential to the core conclusions regarding the predictive capability of the proposed framework.

6. Conclusions

This work presented a fully coupled, multiphysics framework for simulating ICP wind tunnels and predicting the thermo-chemical response of TPS materials under high-enthalpy conditions. By integrating high-fidelity solvers for the plasma, the electromagnetic field, and the material response within a partitioned coupling strategy, the framework enables end-to-end simulation of ICP wind tunnels, from the RF coils to the stagnation region of the material sample. The coupled model successfully captures key magneto-hydrodynamic features of ICP discharges, including vortex-mode recirculation, Joule-heating-driven plasma formation, and Lorentz-force-induced flow confinement. Predictions of plasma jet behavior at low pressures further demonstrate the framework's ability to reproduce the experimentally observed transition from subsonic to supersonic flow. The framework was further validated against cold-wall heat flux measurements and graphite ablation experiments conducted at the Plasmatron X facility at the University of Illinois Urbana-Champaign. Across the three operating conditions, simulated stagnation-point heat fluxes fell within the experimental uncertainty bounds, while the fully coupled ablation simulations reproduced the measured temperature rise and steady-state recession rates with errors below 12% and 10%, respectively. These results confirm the robustness of the coupling strategy and its ability to capture the transient thermal response as well as the long-duration surface recession behavior of ablative materials.

The overall level of agreement obtained in this study is highly encouraging and underscores the effectiveness and robustness of the proposed approach. The modest

discrepancies observed during the early transient heating phase are limited in scope and primarily reflect secondary modeling uncertainties, such as facility power-coupling characterization, simplified surface chemistry assumptions, and minor differences in available material property data. More importantly, the framework introduced in this work establishes a fundamentally new capability for *ab initio*, end-to-end simulation of inductively coupled plasma wind tunnels using only independently measured facility inputs, without empirical tuning or calibration. This represents a significant advance over existing approaches and provides a rigorous, physics-based foundation for high-fidelity and predictive simulations of ICP facilities. As such, the framework enables more reliable interpretation of experimental data and offers a powerful tool for the design, analysis, and optimization of hypersonic material testing campaigns, with clear pathways for future refinements that build upon, rather than redefine, the core methodology.

Acknowledgments

This work is funded by the Vannevar Bush Faculty Fellowship OUSD(RE) Grant No: N00014-21-1-295 with M. Panesi as the Principal Investigator. The work is also supported by the Center for Hypersonics and Entry Systems Studies (CHESS) at UIUC. Computations were performed on Frontera, an HPC resource provided by the Texas Advanced Computing Center (TACC) at The University of Texas at Austin, on allocation CTS20006, with D. Bodony as the Principal Investigator.

Competing interest

The authors declare no competing interests.

References

- [1] Duffa, G., *Ablative thermal protection systems modeling*, American Institute of Aeronautics and Astronautics, Inc., 2013.
- [2] Calomino, A., Bruce, W., Gage, P., Horn, D., Mastaler, M., Rigali, D., Robey, J., Voss, L., Wahlberg, J., and Williams, C., “Evaluation of the NASA arc jet capabilities to support mission requirements,” Tech. rep., 2010.
- [3] Loehle, S., Zander, F., Eberhart, M., Hermann, T., Meindl, A., Massuti-Ballester, B., Leiser, D., Hufgard, F., Pagan, A. S., Herdrich, G., et al., “Assessment of high enthalpy flow conditions for re-entry aerothermodynamics in the plasma wind tunnel facilities at IRS,” *CEAS Space J.*, Vol. 14, No. 2, 2022, pp. 395–406.
- [4] Boulos, M. I., Fauchais, P. L., and Pfender, E., “Handbook of thermal plasmas,” 2023.
- [5] Capponi, L., Oldham, T., Konnik, M., Stephani, K., Bodony, D. J., Panesi, M., Elliott, G. S., and Panerai, F., “Aerothermal characterization of the Plasmatron X wind tunnel: heat flux, stagnation pressure and jet unsteadiness,” *AIAA Paper 2023-1338*.

- [6] Gnoffo, P. A., “Planetary-entry gas dynamics,” *Annu. Rev. Fluid Mech.*, Vol. 31, No. 1, 1999, pp. 459–494.
- [7] Anderson, L., Bartlett, E., Kendall, R., and Nicolet, W., “Further studies of the coupled chemically reacting boundary layer and charring ablator. Part 1-Summary final report,” Tech. rep., 1968.
- [8] Moyer, C. B. and Rindal, R. A., “An analysis of the coupled chemically reacting boundary layer and charring ablator. Part 2-Finite difference solution for the in-depth response of charring materials considering surface chemical and energy balances,” Tech. rep., NASA, 1968.
- [9] Bartlett, E. and Kendall, R., “An analysis of the coupled chemically reacting boundary layer and charring ablator. Part 3-Nonsimilar solution of the multicomponent laminar boundary layer by an integral matrix method,” Tech. rep., NASA, 1968.
- [10] Cooper, J., Salazar, G., and Martin, A., “Numerical investigation of film coefficient approximation for chemically reacting boundary-layer flows,” *J. Thermophys. Heat Transf.*, Vol. 37, No. 3, 2023, pp. 644–655.
- [11] De Müelenaere, J., Magin, T., Lachaud, J., and Mansour, N., “Stagnation line approximation for ablation thermochemistry,” *AIAA Paper 2011-3616*, 2011.
- [12] Milos, F. S., Chen, Y.-K., and Gokcen, T., “Nonequilibrium ablation of phenolic impregnated carbon ablator,” *J. Spacecr. Rockets.*, Vol. 49, No. 5, 2012, pp. 894–904.
- [13] Zibitsker, A. L., McQuaid, J. A., Brehm, C., and Martin, A., “Deviation from equilibrium thermochemistry and aerodynamic heating assumptions in the ablation process of camphor,” *AIAA Paper 2023-3486*, 2023.
- [14] Driver, D., Olson, M., Barnhardt, M., MacLean, M., and MacLean, M., “Understanding high recession rates of carbon ablators seen in shear tests in an arc jet,” *AIAA Paper 2010-1177*.
- [15] Zibitsker, A. L., McQuaid, J. A., Brehm, C., and Martin, A., “Study of a two-dimensional shape change of blunt-body geometries at hypersonic conditions using fully coupled simulation,” *AIAA Paper 2022-4006*, 2022.
- [16] Martin, A. and Boyd, I. D., “Strongly coupled computation of material response and nonequilibrium flow for hypersonic ablation,” *J. Spacecr. Rockets.*, Vol. 52, No. 1, 2015, pp. 89–104.
- [17] Chen, Y.-K., Milos, F. S., and Gokcen, T., “Loosely coupled simulation for two-dimensional ablation and shape change,” *J. Spacecr. Rockets.*, Vol. 47, No. 5, 2010, pp. 775–785.
- [18] Chen, Y.-K., Milos, F., Reda, D., and Stewart, D., “Graphite ablation and thermal response simulation under arc-jet flow conditions,” *AIAA Paper 2003-4042*, 2023.
- [19] Bianchi, D., Nasuti, F., and Martelli, E., “Navier-Stokes simulations of hypersonic flows with coupled graphite ablation,” *J. Spacecr. Rockets.*, Vol. 47, No. 4, 2010, pp. 554–562.
- [20] Bersbach, C. J., Evans, J., Alkandry, H., Ewing, M. E., and Isaac, D. A., “Ablative thermal response numerical modeling under arcjet test conditions,” *J. Thermophys. Heat Transf.*, Vol. 36, No. 3, 2022, pp. 627–636.
- [21] Zibitsker, A. L., McQuaid, J. A., Stern, E. C., Palmer, G. E., Libben, B. J., Brehm, C., and Martin, A., “Finite-rate and equilibrium study of graphite ablation under arc-jet conditions,” *Comput. Fluids.*, Vol. 267, 2023, pp. 106069.
- [22] McClernan, P. G., Schroeder, O. M., Fagnani, A., Knutson, A. L., and Schwartzentruber, T. E., “Finite-Rate Modeling of Air–Carbon Ablation in a Plasma Wind Tunnel,” *J. Thermophys. Heat Transf.*, 2025, pp. 1–14.
- [23] Freeman, M. and Chase, J., “Energy-Transfer mechanism and typical operating characteristics for the thermal rf plasma generator,” *J. Appl. Phys.*, Vol. 39, No. 1, 1968, pp. 180–193.
- [24] Keefer, D., Sprouse, J., and Loper, F., “The electrodeless arc with radial inflow,” *IEEE Trans. Plasma Sci.*, Vol. 1, No. 4, 1973, pp. 71–75.

- [25] Eckert, H., "Analysis of thermal induction plasmas dominated by radial conduction losses," *J. Appl. Phys.*, Vol. 41, No. 4, 1970, pp. 1520–1528.
- [26] Eckert, H. U., "Analytical treatment of radiation and conduction losses in thermal induction plasmas," *J. Appl. Phys.*, Vol. 41, No. 4, 1970, pp. 1529–1537.
- [27] Eckert, H. U., "Analysis of thermal induction plasmas between coaxial cylinders," *J. Appl. Phys.*, Vol. 43, No. 1, 1972, pp. 46–52.
- [28] Eckert, H. U., "Two-dimensional analysis of thermal induction plasmas in finite cylinders," *J. Appl. Phys.*, Vol. 48, No. 4, 1977, pp. 1467–1472.
- [29] Boulos, M. I., "Flow and temperature fields in the fire-ball of an inductively coupled plasma," *IEEE Trans. Plasma Sci.*, Vol. 4, No. 1, 1976, pp. 28–39.
- [30] Mostaghimi, J., Proulx, P., and Boulos, M. I., "Parametric study of the flow and temperature fields in an inductively coupled rf plasma torch," *Plasma Chem. Plasma Process.*, Vol. 4, No. 3, 1984, pp. 199–217.
- [31] Mostaghimi, J., Proulx, P., and Boulos, M. I., "An analysis of the computer modeling of the flow and temperature fields in an inductively coupled plasma," *Numer. Heat Transf.*, Vol. 8, No. 2, 1985, pp. 187–201.
- [32] Mostaghimi, J., Proulx, P., and Boulos, M. I., "A two-temperature model of the inductively coupled rf plasma," *J. Appl. Phys.*, Vol. 61, No. 5, 1987, pp. 1753–1760.
- [33] Proulx, P., Mostaghimi, J., and Boulos, M. I., "Heating of powders in an rf inductively coupled plasma under dense loading conditions," *Plasma Chem. Plasma Process.*, Vol. 7, 1987, pp. 29–52.
- [34] Mostaghimi, J. and Boulos, M. I., "Effect of frequency on local thermodynamic equilibrium conditions in an inductively coupled argon plasma at atmospheric pressure," *J. Appl. Phys.*, Vol. 68, No. 6, 1990, pp. 2643–2648.
- [35] Chen, X. and Pfender, E., "Modeling of RF plasma torch with a metallic tube inserted for reactant injection," *Plasma Chem. Plasma Process.*, Vol. 11, No. 1, 1991, pp. 103–128.
- [36] Panesi, M., Rini, P., Degrez, G., and Chazot, O., "Analysis of chemical nonequilibrium and elemental demixing in plasmatron facility," *J. Thermophys. Heat Transf.*, Vol. 21, No. 1, 2007, pp. 57–66.
- [37] Abeele, D. V. and Degrez, G., "Efficient computational model for inductive plasma flows," *AIAA J.*, Vol. 38, No. 2, 2000, pp. 234–242.
- [38] Utyuzhnikov, S., Konyukhov, A., Rudenko, D., Vasil'evskii, S., Kolesnikov, A., and Chazot, O., "Simulation of subsonic and supersonic flows in inductive plasmatrons," *AIAA J.*, Vol. 42, No. 9, 2004, pp. 1871–1877.
- [39] Kolesnikov, A., "Combined measurements and computations of high enthalpy and plasma flows for determination of TPM surface catalycity," 1999.
- [40] Kolesnikov, A., "The aerothermodynamic simulation in-and supersonic high-enthalpy jets: experiment and theory," *Aerothermodynamics for space vehicles, Proceedings of the 2nd European Symposium held in ESTEC, Noordwijk, The Netherlands, 21-25 November, 1994, Edited by JJ Hunt, Published by European Space Agency (ESA)(Paris), 1995, p. 583*, Vol. 367, 1995, p. 583.
- [41] Gordeev, A., "Methodology, Technical Approach and Measurement Techniques for Testing of TPM Thermal Protection Materials in IPM Plasmatrons," 2000.
- [42] Vasil'Evskii, S., Kolesnikov, A., and Yakushin, M., "Mathematical models for plasma and gas flows in induction plasmatrons," *Mol. Phys. Hyperson. Flows*, Springer, 1996, pp. 495–504.
- [43] Kolesnikov, A., Gordeev, A., Vasil'evskii, S., and Sakharov, V., "Heat Transfer in Nonequilibrium Dissociated Nitrogen Jets: Experiments in RF-Plasmatron and Numerical Modeling," *Fiziko-khimicheskaya kinetika v gazovoy dinamike [Physical-Chemical Kinetics in Gas Dynamics]*,

Vol. 17, No. 2, 2016.

- [44] Bykova, N., Vasilevskii, S. A., and Kolesnikov, A. F., “The effect of radiation on the spatial distribution of the temperature of subsonic flows of induction plasma,” *High Temp.*, Vol. 42, No. 1, 2004, pp. 12–19.
- [45] Munafò, A., Kumar, S., and Panesi, M., “Self-consistent modeling of inductively coupled plasma discharges,” *AIP Conf. Proc.*, Vol. 2996, AIP Publishing, 2024.
- [46] Zhang, W., Lani, A., and Panesi, M., “Analysis of non-equilibrium phenomena in inductively coupled plasma generators,” *Phys. Plasmas*, Vol. 23, No. 7, 2016, pp. 073512.
- [47] Munafò, A., Alfuhaid, S., Cambier, J.-L., and Panesi, M., “A tightly coupled non-equilibrium model for inductively coupled radio-frequency plasmas,” *J. Appl. Physics*, Vol. 118, No. 13, 2015, pp. 133303.
- [48] Lei, F., Li, X., Liu, Y., Liu, D., Yang, M., and Yu, Y., “Simulation of a large size inductively coupled plasma generator and comparison with experimental data,” *AIP Adv.*, Vol. 8, No. 1, 2018.
- [49] Kumar, S., Munafò, A., Jo, S. M., and Panesi, M., “Investigation of non-equilibrium phenomena in nitrogen RF inductively coupled plasma discharges: a state-to-state approach,” *J. Phys. D: Appl. Phys.*, Vol. 58, No. 2, 2024, pp. 025204.
- [50] Kumar, S., Munafò, A., Jo, S. M., and Panesi, M., “Electronic-state-resolved non-equilibrium analysis of ICP discharges,” *AIP Conf. Proc.*, Vol. 2996, AIP Publishing, 2024.
- [51] Laux, C. O., Pierrot, L., and Gessman, R. J., “State-to-state modeling of a recombining nitrogen plasma experiment,” *Chem. Phys.*, Vol. 398, 2012, pp. 46–55.
- [52] Panesi, M., Jaffe, R. L., Schwenke, D. W., and Magin, T. E., “Rovibrational internal energy transfer and dissociation of $N_2(^1\Sigma_g^+) - N(^4S_u)$ system in hypersonic flows,” *J. Chem. Phys.*, Vol. 138, No. 4, 2013.
- [53] Colonna, G., Laporta, V., Celiberto, R., Capitelli, M., and Tennyson, J., “Non-equilibrium vibrational and electron energy distributions functions in atmospheric nitrogen ns pulsed discharges and μs post-discharges: the role of electron molecule vibrational excitation scaling-laws,” *Plasma Sources Sci. Technol.*, Vol. 24, No. 3, 2015, pp. 035004.
- [54] Laporta, V., Heritier, K., and Panesi, M., “Electron-vibration relaxation in oxygen plasmas,” *Chem. Phys.*, Vol. 472, 2016, pp. 44–49.
- [55] Capitelli, M., Ferreira, C. M., Gordiets, B. F., and Osipov, A. I., *Plasma kinetics in atmospheric gases*, Vol. 31, Springer Science & Business Media, 2013.
- [56] Park, C., *Nonequilibrium hypersonic aerothermodynamics*, 1990.
- [57] Park, C., “Review of chemical-kinetic problems of future NASA missions. I-Earth entries,” *J. Thermophys. Heat transfer*, Vol. 7, No. 3, 1993, pp. 385–398.
- [58] Gnoffo, P. A., *Conservation equations and physical models for hypersonic air flows in thermal and chemical nonequilibrium*, Vol. 2867, NASA Technical Paper, 1989.
- [59] Park, C., Jaffe, R. L., and Partridge, H., “Chemical-kinetic parameters of hyperbolic earth entry,” *J. Thermophys. Heat Transf.*, Vol. 15, No. 1, 2001, pp. 76–90.
- [60] Atsuchi, N., Shigeta, M., and Watanabe, T., “Modeling of non-equilibrium argon–oxygen induction plasmas under atmospheric pressure,” *Int. J. Heat Mass Transf.*, Vol. 49, No. 5-6, 2006, pp. 1073–1082.
- [61] Yu, M., Ma, L., and Liu, K., “Effects of the Nonequilibrium Model and the Discharge Frequency on an Argon Inductively Coupled Plasma Simulation,” *J. Korean Phys. Soc.*, Vol. 75, 2019, pp. 131–137.
- [62] Munafò, A., Chiodi, R., Kumar, S., Le Maout, V., Stephani, K. A., Panerai, F., Bodony, D. J., and Panesi, M., “A Multi-Physics Modeling Framework for Inductively Coupled Plasma Wind Tunnels,” *AIAA Paper 2022-1011*, 2022.

- [63] Sun, J., Shi, J., Li, Y., Liu, Y.-Q., Zhao, Y., Zhang, X., Cai, H., Zhu, X., Sun, X., Yin, H., et al., “Validation of inductively coupled plasma simulation model by laser Thomson scattering experiment,” *J. Plasma Phys.*, Vol. 89, No. 4, 2023, pp. 905890409.
- [64] Munafò, A., Kumar, S., Jo, S. M., and Panesi, M., “Hegel: a high-fidelity flexible software for hypersonics and plasma simulations,” *AIAA Paper 2024-0449*.
- [65] Kumar, S., Munafò, A., Le Maout, V., Mansour, N., and Panesi, M., “Self-consistent magneto-hydrodynamic modeling of ICP discharges,” *AIAA Paper 2022-1619*.
- [66] Munafò, A. and Panesi, M., “Plato: a high-fidelity library for multicomponent gases and plasmas,” *J. Thermophys. Heat Transfer*, Vol. 39, No. 4, 2025, pp. 850–870.
- [67] Chiodi, R. M., Stephani, K. A., Panesi, M., and Bodony, D. J., “CHyPS: A high-order material response solver for ablative thermal protection systems,” *AIAA Paper 2022-1501*.
- [68] Anderson, R., Andrej, J., Barker, A., Bramwell, J., Camier, J.-S., Dobrev, J. C. V., Dudouit, Y., Fisher, A., Kolev, T., Pazner, W., Stowell, M., Tomov, V., Akkerman, I., Dahm, J., Medina, D., and Zampini, S., “MFEM: A Modular Finite Element Library,” *Comput. Math. with Appl.*, Vol. 81, 2021, pp. 42–74.
- [69] Lachaud, J. and Mansour, N. N., “Porous-material analysis toolbox based on OpenFOAM and applications,” *J. Thermophys. Heat Transf.*, Vol. 28, No. 2, 2014, pp. 191–202.
- [70] Weng, H. and Martin, A., “Multidimensional modeling of pyrolysis gas transport inside charring ablative materials,” *J. Thermophys. Heat Transf.*, Vol. 28, No. 4, 2014, pp. 583–597.
- [71] Bungartz, H.-J., Lindner, F., Gatzhammer, B., Mehl, M., Scheufele, K., Shukaev, A., and Uekermann, B., “preCICE—a fully parallel library for multi-physics surface coupling,” *Comput. Fluids*, Vol. 141, 2016, pp. 250–258.
- [72] Chourdakis, G., Davis, K., Rodenberg, B., Schulte, M., Simonis, F., Uekermann, B., Abrams, G., Bungartz, H., Cheung Yau, L., Desai, I., Eder, K., Hertrich, R., Lindner, F., Rusch, A., Sashko, D., Schneider, D., Totounferoush, A., Volland, D., Vollmer, P., and Koseomur, O., “preCICE v2: A sustainable and user-friendly coupling library [version 2; peer review: 2 approved],” *Open Research Europe*, Vol. 2, No. 51, 2022.
- [73] Spekrijse, S. P., Prananta, B. B., and Kok, J. C., “A simple, robust and fast algorithm to compute deformations of multi-block structured grids,” National Aerospace Laboratory NLR, 2002.
- [74] Eriksson, L., “Generation of boundary-conforming grids around wing-body configurations using transfinite interpolation,” *AIAA J.*, Vol. 20, No. 10, 1982, pp. 1313–1320.
- [75] Thompson, R. and Gnoffo, P., “Implementation of a blowing boundary condition in the LAURA code,” *AIAA Paper 2008-1243*, 2008.
- [76] Oruganti, S., Kumar, S., Le Maout, V., Capponi, L., Munafò, A., Bodony, D. J., Panesi, M., Panerai, F., Mansour, N., and Fraile Izquierdo, S., “Modeling instrumented test articles for Plasmatron X aerothermal environment,” *AIAA Paper 2023-3327*, 2023.
- [77] Belevitch, V., “Lateral skin effect in a flat conductor,” *Philips Tech. Rev.*, Vol. 32, No. 6, 1971, pp. 221–231.
- [78] Blackwell, A. E., Rotunno, A. P., and Aubin, S., “Demonstration of the lateral AC skin effect using a pickup coil,” *Am. J. Phys.*, Vol. 88, No. 8, 2020, pp. 676–684.
- [79] Van Leer, B., “Towards the ultimate conservative difference scheme. V. A second-order sequel to Godunov’s method,” *J. Comput. Phys.*, Vol. 32, No. 1, 1979, pp. 101–136.
- [80] Liou, M.-S., “A sequel to AUSM, Part II: AUSM+—up for all speeds,” *J. Comput. Phys.*, Vol. 214, No. 1, 2006, pp. 137–170.
- [81] Saad, Y., “A flexible inner-outer preconditioned GMRES algorithm,” *SIAM J. Sci. Comput.*, Vol. 14, No. 2, 1993, pp. 461–469.
- [82] McCormick, S. F., *Multigrid methods*, SIAM, 1987.
- [83] Boulos, M. I., “The inductively coupled RF (radio frequency) plasma,” *Pure Appl. Chem.*, Vol. 57,

No. 9, 1985, pp. 1321–1352.

- [84] Eckert, H. U., “The induction arc: a state of the art review,” *High Temp. Sci.*, Vol. 6, 1974, pp. 99–133.
- [85] Capponi, L., Padovan, A., Elliott, G. S., Panesi, M., Bodony, D. J., and Panerai, F., “Multi-domain analysis and prediction of inductively coupled plasma jet dynamics via high-speed imaging of visible light emission,” *Exp. Therm. Fluid Sci.*, Vol. 157, 2024, pp. 111232.
- [86] Jo, S. M., Kumar, S., Le Maout, V., Munafò, A., and Panesi, M., “Multi-Fidelity Modeling Framework for Radiative Transfer in Hypersonic Atmospheric Entry,” *AIAA Paper 2023-1730*, 2023.
- [87] Franco, M., Capponi, L., Oruganti, S., Elliott, G., and Panerai, F., “Investigation of slug calorimeter heat flux measurements in the Plasmatron X wind tunnel,” *AIAA Paper 2024-1900*.
- [88] Meyers, J. M., Schindler, J., Ballou, I., and Fletcher, D., “Progress on Carbon Nitridation and Nitrogen Catalysis Studies in an Inductively Coupled Plasma Facility,” *AIAA Paper 2022-3577*.
- [89] Oruganti, S., Capponi, L., Ringel, B., Oldham, T., Panesi, M., Elliott, G. S., Izquierdo, S. F., Mansour, N. N., and Panerai, F., “In-Depth Ablation of Charring Ablators for Titan and Earth Atmospheric Entries,” *Available at SSRN 5740826*.
- [90] Fagnani, A., Le Quang Huy, D., Helber, B., Demange, S., Turchi, A., Chazot, O., and Hubin, A., “Investigation of a free-stream air plasma flow by optical emission spectroscopy and comparison to magnetohydrodynamics simulations,” *AIAA Paper 2020-0382*, 2020.